

Simulation of premixed combustion with varying equivalence ratio in gas turbine combustor

S. Ruan¹ and N. Swaminathan²
*Engineering Department, University of Cambridge,
Trumpington Street, Cambridge CB2 1PZ, UK*

M. Isono³ and T. Saitoh⁴ and K. Saitoh⁵
Mitsubishi Heavy Industries, Takasago, Japan

(Dated: Submitted 10th July 2014, Revised 12th November 2014)

RANS simulation of a gas turbine combustor with complex geometry is performed. The turbulence is modelled using a two-equation approach. The scalar mixing and combustion is modelled using a flamelet based approach for partially premixed combustion. In this approach transport equations to described scalar mixing and reacting fields and their statistical interactions are solved along with standard conservation equations. The boundary conditions are specified using measured values. The computed spatial variations of averaged temperature and dry mole fractions of various scalars, including CO and NOx, compared quite well with measured values. The results of this combustion model are compared to the eddy-dissipation-concept (EDC) model commonly used for gas turbine combustion calculation and this comparison showed that the results of partially premixed combustion model is improved considerably.

¹ Research Associate, Engineering Department, University of Cambridge.

² Professor, Engineering Department, University of Cambridge.

³ Deputy Manager, Mitsubishi Heavy Industries Ltd, Takasago R&D center, Takasago, Japan

⁴ Deputy Manager, Mitsubishi Heavy Industries Ltd, Takasago R&D center, Takasago, Japan

⁵ Research Manager, Mitsubishi Heavy Industries Ltd, Takasago R&D center, Takasago, Japan

I. Introduction

Lean combustion technology has attracted much attention as it can improve fuel economy while reducing pollutants emission and thereby improving environmental impacts of gas turbine combustion. Unfortunately lean flames are susceptible to combustion instability issues, which can be addressed to some degree by introducing suitable gradients of mixture fraction or equivalence ratio in critical regions of combustor so that burning of relatively rich mixture can support burning of lean mixture in an adjacent region. The combustion of variable equivalence ratio mixture is generally known as partially premixed combustion (PPC) if the variation of local equivalence ratio extends beyond the flammability limits for a given thermochemical conditions. If the range is within the flammability limits then it is commonly known as stratified combustion. The physics of PPC is more complex than the classical premixed and non-premixed combustion modes since turbulence, molecular diffusion, chemical reactions and heat release are strongly coupled with one another locally. This strong coupling offers considerable challenge for modelling of PPC, especially in the closure of mean chemical reaction rate.

One simple model is the Eddy Break Up (EBU) [1] or Eddy Dissipation Concept [2]. This type of modelling assumes that the mean reaction rate is limited by the rate of turbulence mixing of relevant scalars and this mixing rate is typically modelled using the inverse of the turbulence time scale, $\tilde{k}/\tilde{\epsilon}$, where \tilde{k} and $\tilde{\epsilon}$ are the Favre averaged turbulence kinetic energy and its dissipation rate respectively. Despite its apparent limitations such as no fuel dependence, fast chemistry limits and model parameters requiring tuning on a case-by-case basis to produce reasonable results, this model is commonly used for gas turbine combustion calculations because of its simplicity and affordable computational cost.

The flamelets based method [3–7] is a popular approach to include finite rate chemistry effects. In this approach, the turbulent flame is considered as an ensemble of laminar flamelets and the mean reaction rate can be expressed as

$$\bar{\omega} = \int_0^1 \int_0^1 \dot{\omega}(\zeta, \xi) P(\zeta, \xi) d\zeta d\xi, \quad (1)$$

where ξ and ζ are sample space variables for mixture fraction, Z , and a reaction progress variable, c . The symbol $\dot{\omega}(\zeta, \xi)$ denotes the flamelet reaction rate. The mixture fraction and progress variable

used in this study will be defined later in Section II B.

The joint PDF, $P(\zeta, \xi)$ is commonly modelled as the product of two marginal PDFs, $P(\xi)P(\zeta)$, after assuming that ξ and ζ are statistically independent. A Beta function for ξ and a double delta function for ζ were the common choices [8]. The assumption of statistical independence for ξ and ζ is not always justified [9] and their strong coupling in PPC is well established [9–11].

Recently Darbyshire and Swaminathan [12] developed to relax this assumption by including the $Z - c$ correlation with a *copula*. Partially premixed combustion can include both premixed and non-premixed combustion and thus one must include both of them. For example, in practical engines this requirement becomes much more relevant because of the presence of non-premixed pilot flame. Combustion modelling framework allowing these two modes of combustion was developed by Ruan et al. [13] and has been used in earlier studies of laboratory scale flames. The aim of this study is to apply this modelling to calculate premixed combustion with varying equivalence ratio inside a gas turbine combustor with complex geometry and flow conditions. In particular, the interest is to investigate the model efficacy to estimate CO and NOx variation inside the combustor and to compare with experimental measurement.

The paper is organized as follows. Section II outlines the modelling methodology used in this study. Section III describes a test case of a practical gas turbine combustor along with a brief description of the experimental methods and measurement techniques. Section IV presents detailed numerical implementation of the model for the test case. This is followed by results and discussion section. The final section provide a summary of conclusions.

II. Modelling Framework

A. Governing Equations

The equations for conservation of Favre averaged mass, momentum and enthalpy are required and they are given below:

$$\frac{\partial \bar{\rho}}{\partial t} + \frac{\partial \bar{\rho} \tilde{u}_i}{\partial x_i} = 0, \quad (2)$$

$$\frac{\partial \bar{\rho} \tilde{u}_i}{\partial t} + \frac{\partial \bar{\rho} \tilde{u}_i \tilde{u}_k}{\partial x_k} = -\frac{\partial \bar{p}}{\partial x_i} + \frac{\partial}{\partial x_k} \left(\overline{\tau_{ik}} - \bar{\rho} \widetilde{u_i'' u_k''} \right), \quad (3)$$

$$\frac{\partial \bar{\rho} \tilde{h}}{\partial t} + \frac{\partial \bar{\rho} \tilde{u}_k \tilde{h}}{\partial x_k} = \frac{\partial}{\partial x_k} \left[\frac{\mu}{Sc_h} \frac{\partial \tilde{h}}{\partial x_k} - \overline{\rho u_k'' h''} \right]. \quad (4)$$

The standard nomenclature is used for the above equations and the symbol Sc_i denotes the molecular Schmidt number for the scalar i . The total enthalpy includes the sensible and chemical contributions and thus the mixture temperature, \tilde{T} , is obtained using \tilde{h} as will be explained later in section II B.

The turbulence is modelled using a two equations, \tilde{k} - $\tilde{\varepsilon}$, modelling approach [14] as it is widely used because of its simplicity, low computational cost and reasonable accuracy for a wide range of flow configurations. The Favre averaged turbulent kinetic energy \tilde{k} and its dissipation rate $\tilde{\varepsilon}$ are computed using [8, 15]

$$\frac{\partial \bar{\rho} \tilde{k}}{\partial t} + \frac{\partial \bar{\rho} \tilde{u}_i \tilde{k}}{\partial x_i} = \frac{\partial}{\partial x_j} \left[\left(\mu + \frac{\mu_t}{Sc_k} \right) \frac{\partial \tilde{k}}{\partial x_j} \right] + P_k - \bar{\rho} \tilde{\varepsilon}, \quad (5)$$

$$\frac{\partial \bar{\rho} \tilde{\varepsilon}}{\partial t} + \frac{\partial \bar{\rho} \tilde{u}_i \tilde{\varepsilon}}{\partial x_i} = \frac{\partial}{\partial x_j} \left[\left(\mu + \frac{\mu_t}{Sc_\varepsilon} \right) \frac{\partial \tilde{\varepsilon}}{\partial x_j} \right] - C_{\varepsilon 1} \frac{\tilde{\varepsilon}}{\tilde{k}} P_k - C_{\varepsilon 2} \bar{\rho} \frac{\tilde{\varepsilon}^2}{\tilde{k}}, \quad (6)$$

$$P_k = -\bar{\rho} \widetilde{u_i'' u_j''} \frac{\partial \tilde{u}_i}{\partial x_j} - \overline{u_i'' \frac{\partial \bar{p}}{\partial x_i}} + \overline{p' \frac{\partial u_i''}{\partial x_i}}. \quad (7)$$

The pressure dilatation, $\overline{p' \partial u_i'' / \partial x_i}$, is modelled using [16]

$$\overline{p' \frac{\partial u_i''}{\partial x_i}} = 0.5 (\tau S_L^0)^2 \bar{\omega}_c. \quad (8)$$

The effects of mean pressure gradient is included by modelling $\overline{u_i''}$ as [8]

$$\overline{u_i''} = \widetilde{u'' c''} \frac{\tau}{(1 + \tau \tilde{c})}. \quad (9)$$

The symbol τ and S_L^0 are the heat release parameter and the laminar flame speed. The scalar flux $\widetilde{u'' c''}$ is modelled using gradient hypothesis. The reaction rate needs to be modelled.

The turbulent eddy viscosity is calculated using $\mu_t = C_\mu \bar{\rho} \tilde{k}^2 / \tilde{\varepsilon}$ with $C_\mu = 0.09$. Standard model constants $C_{\varepsilon 1} = 1.44$ and $C_{\varepsilon 2} = 1.92$ are used in this study.

B. Combustion Modelling

The turbulent combustion of partially premixed mixture is modelled by solving the transport equations for Favre averaged mixture fraction \tilde{Z} , progress variable \tilde{c} and their variances $\widetilde{Z''^2}$, $\widetilde{c''^2}$. This same model has been used in previous study of laboratory scale flames [12, 13]. The Favre averaged mixture fraction \tilde{Z} and its variance $\widetilde{Z''^2}$ are useful to track the spatio-temporal evolution of the scalar mixing field. The mixture fraction is defined as [17]

$$Z \equiv \frac{2Y_C/W_C + Y_H/2W_H + (Y_{O,2} - Y_O)/W_O}{2Y_{C,1}/W_C - Y_{O,1}/W_O + Y_{H,1}/2W_H + Y_{O,2}/W_O}. \quad (10)$$

where the mass fraction of an element i and its atomic mass are denoted as Y_i and W_i respectively. Here, the carbon, hydrogen and oxygen elements are denoted using subscript C, H and O. The subscripts 1 and 2 denote the fuel and oxidiser streams respectively. Thus, $Z = 1$ implies fuel steam regardless of its dilution and $Z = 0$ implies the air stream.

The reaction progress variable indicating the progress of chemical reaction may be defined using temperature, species mass fraction, etc. However, its specific definition depends on the problem of interest. Here for methane-air mixture, the sum of CO and CO₂ mass fractions, $\psi = Y_{CO} + Y_{CO_2}$, is used for methane combustion and this definition is chosen because it allows a unique mapping of flamelet quantities with progress variable [18], c , defined as

$$c = \frac{\psi}{\psi^{Eq}(Z)}, \quad (11)$$

where $\psi^{Eq}(Z)$ is the equilibrium value of ψ for the local mixture fraction, Z , so that c is bounded between 0 and 1.

The transport equations for \tilde{Z} , \tilde{c} , $\widetilde{Z''^2}$ and $\widetilde{c''^2}$ are [8, 19]

$$\frac{\partial \tilde{\rho} \tilde{Z}}{\partial t} + \frac{\partial \tilde{\rho} \tilde{u}_k \tilde{Z}}{\partial x_k} = \frac{\partial}{\partial x_k} \left(\overline{\rho D \frac{\partial \tilde{Z}}{\partial x_k}} - \overline{\rho u_k'' \tilde{Z}''} \right), \quad (12)$$

$$\begin{aligned} \frac{\partial \tilde{\rho} \widetilde{Z''^2}}{\partial t} + \frac{\partial \tilde{\rho} \tilde{u}_k \widetilde{Z''^2}}{\partial x_k} &= \frac{\partial}{\partial x_k} \left(\overline{\rho D \frac{\partial \widetilde{Z''^2}}{\partial x_k}} - \overline{\rho u_k'' \widetilde{Z''^2}''} \right) \\ &\quad - 2 \tilde{\rho} \tilde{\epsilon}_{ZZ} - 2 \overline{\rho u_k'' \tilde{Z}''} \frac{\partial \tilde{Z}}{\partial x_k}, \end{aligned} \quad (13)$$

$$\frac{\partial \bar{\rho} \tilde{c}}{\partial t} + \frac{\partial \bar{\rho} \tilde{u}_k \tilde{c}}{\partial x_k} = \frac{\partial}{\partial x_k} \left(\overline{\rho D \frac{\partial c}{\partial x_k}} - \overline{\rho u_k'' c''} \right) + \bar{\omega}_c^*, \quad (14)$$

$$\begin{aligned} \frac{\partial \bar{\rho} \tilde{c}''^2}{\partial t} + \frac{\partial \bar{\rho} \tilde{u}_k \tilde{c}''^2}{\partial x_k} &= \frac{\partial}{\partial x_k} \left(\overline{\rho D \frac{\partial c''^2}{\partial x_k}} - \overline{\rho u_k'' c''^2} \right) \\ &\quad - 2 \bar{\rho} \tilde{\epsilon}_{cc} - 2 \overline{\rho u_k'' c''} \frac{\partial \tilde{c}}{\partial x_k} + 2 \overline{c'' \tilde{\omega}_c^*}, \end{aligned} \quad (15)$$

where $\bar{\omega}_c^*$ denotes the total reaction rate to be discussed in detailed later. Since the mixing and chemical reaction are strongly coupled in partially premixed combustion, one can not ignore their statistical correlation and thus the covariance $\overline{c'' \tilde{Z}''}$ must also be included in the analysis. This equation is written as [12, 13]

$$\begin{aligned} \frac{\partial \bar{\rho} \tilde{c}'' \tilde{Z}''}{\partial t} + \frac{\partial \bar{\rho} \tilde{u}_k \tilde{c}'' \tilde{Z}''}{\partial x_k} &= \frac{\partial}{\partial x_k} \left(\overline{\rho D \frac{\partial c'' \tilde{Z}''}{\partial x_k}} - \overline{\rho u_k'' c'' \tilde{Z}''} \right) \\ &\quad - 2 \bar{\rho} \tilde{\epsilon}_{cZ} - \overline{\rho u_k'' c''} \frac{\partial \tilde{Z}}{\partial x_k} - \overline{\rho u_k'' \tilde{Z}''} \frac{\partial \tilde{c}}{\partial x_k} + \overline{c'' \tilde{\omega}_c^*}. \end{aligned} \quad (16)$$

The various turbulent scalar fluxes are modelled using gradient flux approximation, for example $\overline{u_k'' \tilde{Z}''} = -D_t \partial \tilde{Z} / \partial x_k$ with a turbulent diffusivity of D_t . The turbulent scalar flux of c can become counter gradient under appropriate condition, and this can be modelled using a second order closure with additional computational effort. Here, a gradient flux approximation is used to avoid the uncertainties that could arise by using a second order scalar flux modelling. Furthermore, this scalar flux is known to be gradient in turbulent premixed combustion at high Reynolds number. A turbulent Schmidt number of 0.7 is used for all scalar in this study.

The Favre averaged dissipation rate of scalar fluctuation, $\tilde{\epsilon}_{ZZ}$ in Eq.(13), $\tilde{\epsilon}_{cc}$ in Eq.(15) and $\tilde{\epsilon}_{cZ}$ in Eq.(16) require modelling. They are defined as $\tilde{\epsilon}_{ZZ} \equiv \overline{\rho D (\nabla Z'' \cdot \nabla Z'') / \bar{\rho}}$, $\tilde{\epsilon}_{cc} \equiv \overline{\rho D (\nabla c'' \cdot \nabla c'') / \bar{\rho}}$ and $\tilde{\epsilon}_{cZ} \equiv \overline{\rho D (\nabla c'' \cdot \nabla Z'') / \bar{\rho}}$. Simple algebraic models assuming a proportionality between scalar and turbulence time scales can be written as $\tilde{\epsilon}_{ZZ} \simeq C_{d1} \left(\tilde{\epsilon} / \tilde{k} \right) \tilde{Z}''^2$ and $\tilde{\epsilon}_{cZ} \simeq C_{d2} \left(\tilde{\epsilon} / \tilde{k} \right) \tilde{c}'' \tilde{Z}''$, where C_{d1} and C_{d2} are model constant and they are taken to be unity here.

An algebraic model for $\tilde{\epsilon}_{cc}$ is used following [9, 20] as given below

$$\bar{\rho} \tilde{\epsilon}_{cc} = \overline{\rho D (\nabla c'' \cdot \nabla c'')} \simeq \frac{\bar{\rho}}{\beta'} \left([2K_c^* - \tau C_4] \frac{S_L^0}{\delta_L^0} + C_3 \frac{\tilde{\epsilon}}{\tilde{k}} \right) \tilde{c}''^2, \quad (17)$$

with

$$C_3 = \frac{1.5\sqrt{\text{Ka}}}{1 + \sqrt{\text{Ka}}} \quad \text{and} \quad C_4 = 1.1(1 + \text{Ka})^{-0.4}. \quad (18)$$

The parameter $\tau = (T_b(Z) - T_u)/T_u$ is the normalised temperature rise, with T_b and T_u indicating burnt and unburnt mixture temperature. The heat release parameter varies with the mixture fraction. The model constant β' taken to be 6.7 and $K_c^* \approx 0.8\tau$ for methane-air flame [20]. The unstrained laminar flame speed and its thermal thickness for a mixture having the mixture fraction value of Z are denoted respectively as S_L^0 and δ_L^0 . The Karlovitz number, Ka, is defined as

$$\text{Ka} \equiv \frac{t_c}{t_k} \simeq \frac{\delta(Z)/S_L^0(Z)}{\sqrt{\nu/\tilde{\varepsilon}}}, \quad (19)$$

where t_k is the Kolmogorov time scale, t_c is the chemical time scale defined as δ/S_L^0 with δ as the Zeldovich flame thickness which is related to the thermal thickness through $\delta_L^0/\delta \approx 2(1 + \tau)^{0.7}$, and ν is the kinematic viscosity. In Eqs.(17)-(19), the local value of \tilde{Z} is used in this study for simplicity.

The mean reaction rate, $\overline{\dot{\omega}_c^*}$, in the transport equation for c can be written as [10, 21–23]

$$\overline{\dot{\omega}_c^*} = \frac{1}{\overline{\partial\psi/\partial c}} \left(\overline{\dot{\omega}_\psi + 2\rho N_{cZ} \frac{\partial^2\psi}{\partial c\partial Z} + \rho N_{ZZ} \frac{\partial^2\psi}{\partial Z^2} + \rho N_{cc} \frac{\partial^2\psi}{\partial c^2}} \right), \quad (20)$$

where $\dot{\omega}_\psi = \dot{\omega}_{\text{CO}} + \dot{\omega}_{\text{CO}_2}$ is the reaction rate for ψ . The three instantaneous scalar dissipation rates are defined as $N_{ZZ} = D(\nabla Z \cdot \nabla Z)$, $N_{Zc} = D(\nabla c \cdot \nabla Z)$ and $N_{cc} = D(\nabla c \cdot \nabla c)$. The derivatives in Eq. (20) become

$$\frac{\partial\psi}{\partial Z} = c \frac{d\psi^{Eq}}{dZ} \quad \Rightarrow \quad \frac{\partial^2\psi}{\partial Z^2} = c \frac{d^2\psi^{Eq}}{dZ^2}, \quad (21)$$

$$\frac{\partial\psi}{\partial c} = \psi^{Eq} \quad \Rightarrow \quad \frac{\partial^2\psi}{\partial c^2} = 0, \quad \text{and} \quad \frac{\partial^2\psi}{\partial Z\partial c} = \frac{d\psi^{Eq}}{dZ}. \quad (22)$$

Substituting these derivatives into Eq. (20) and then averaging the resulting equation one obtains

$$\overline{\dot{\omega}_c^*} = \overline{\dot{\omega}_c} + \underbrace{\overline{\rho N_{ZZ} \frac{c}{\psi^{Eq}} \frac{d^2\psi^{Eq}}{dZ^2}}}_{\overline{\dot{\omega}_{\text{np}}}} + \underbrace{\overline{2\rho N_{Zc} \frac{1}{\psi^{Eq}} \frac{d\psi^{Eq}}{dZ}}}_{\overline{\dot{\omega}_{\text{cdr}}}}. \quad (23)$$

The first part signifies the contribution of premixed mode combustion, the second part, $\overline{\dot{\omega}_{\text{np}}}$, signifies the contributions from non-premixed mode and the third part, $\overline{\dot{\omega}_{\text{cdr}}}$, denotes a contribution resulting

from interactions of Z and c gradients. Previous studies [9, 22] showed that the cross dissipation contribution is an order of magnitude smaller than the contributions from the other two terms and thus $\overline{\dot{\omega}_{\text{cdr}}}$ is neglected from further consideration in this work. The other two terms are modelled as follows.

The first term of Eq. (23) is modelled as [13]

$$\overline{\dot{\omega}_c} = \bar{\rho} \int_0^1 \int_0^1 \left[\frac{\dot{\omega}_c(\zeta, \xi)}{\rho(\zeta, \xi)} \right] \tilde{P}(\zeta, \xi) \, d\zeta \, d\xi, \quad (24)$$

where $\bar{\rho}$ is the mean local mixture density obtained as described in the later part of this subsection. The flamelet reaction rate, $\dot{\omega}_c(\zeta, \xi)$, and mixture density, $\rho(\zeta, \xi)$, are obtained from laminar unstrained premixed flame calculation. The Favre joint PDF, $\tilde{P}(\zeta, \xi)$, including Z - c correlation is calculated using the copula method described in [12, 13]. This correlation is calculated using the covariance, $\widetilde{c''Z''}$, obtained from its transport equations, Eq. (16).

The second term, $\overline{\dot{\omega}_{\text{np}}}$, denoting contributions of non-premixed mode combustion is modelled as [13]

$$\overline{\dot{\omega}_{\text{np}}} \simeq \bar{\rho} \tilde{c} \tilde{\epsilon}_{ZZ} \int_0^1 \frac{1}{\psi^{Eq}(\xi)} \frac{d^2 \psi^{Eq}(\xi)}{dZ^2} \tilde{P}_\beta(\xi) \, d\xi. \quad (25)$$

Strictly, one must include the contributions of three scalar dissipation rates in Eq. (20) at the flamelet level to close $\overline{c''\dot{\omega}_c^{*''}}$ and $\overline{Z''\dot{\omega}_c^{*''}}$ in Eqs. (15) and (16) respectively. This would need a multi-dimensional (in physical space) flamelet or alternatively the multidimensional flamelet generated manifolds with the three dissipation rates as controlling parameters [24]. This adds further complexity into the modelling and so the approximations $\overline{c''\dot{\omega}_c^{*''}} \approx \overline{c''\dot{\omega}_c''}$ and $\overline{Z''\dot{\omega}_c^{*''}} \approx \overline{Z''\dot{\omega}_c''}$ are made here for the sake of simplicity. The validity of this approximation was shown to be acceptable in [13] and it can also be adjudged using comparisons with experimental measurements to be discussed in later part of this paper. The closure models for the above two terms are then written as [12, 13]:

$$\overline{c''\dot{\omega}_c''} \approx \overline{c''\dot{\omega}_c} = \bar{\rho} \int_0^1 \int_0^1 (\zeta - \tilde{\zeta}) \frac{\dot{\omega}_c(\xi, \zeta)}{\rho(\xi, \zeta)} \tilde{P}(\xi, \zeta) \, d\xi \, d\zeta, \quad (26)$$

$$\overline{Z''\dot{\omega}_c''} \approx \overline{Z''\dot{\omega}_c} = \bar{\rho} \int_0^1 \int_0^1 (\xi - \tilde{\xi}) \frac{\dot{\omega}_c(\xi, \zeta)}{\rho(\xi, \zeta)} \tilde{P}(\xi, \zeta) \, d\xi \, d\zeta. \quad (27)$$

The temperature, \tilde{T} , is calculated using the total enthalpy \tilde{h} computed in the simulation using its transport equation Eq.(4). This enthalpy includes the sensible and chemical parts as

$$\tilde{h} = c_{p,\text{mix}}(\tilde{T} - T_0) + \Delta h_{f,\text{mix}}^0, \quad (28)$$

where $T_0 = 298$ K is a reference temperature. The mixture averaged specific heat capacity $c_{p,\text{mix}}$ and the enthalpy of formation $\Delta h_{f,\text{mix}}^0$ are calculated as

$$c_{p,\text{mix}} = \int_0^1 \int_0^1 c_p^e(\xi, \zeta) \tilde{P}(\xi, \zeta) d\zeta d\xi, \quad (29)$$

$$\Delta h_{f,\text{mix}}^0 = \sum \int_0^1 \int_0^1 Y_i \Delta h_{f,i}^0 \tilde{P}(\xi, \zeta) d\zeta d\xi, \quad (30)$$

The $c_{p,\text{mix}}$ given in Eq. (28) includes its temperature dependence through Eq. (29) while simulating turbulent combustion. An effective specific heat capacity, defined as $c_p^e = \left(\int_{T_0}^{T_1} c_p dT \right) / (T_1 - T_0)$ is used to include the temperature dependence at the flamelet level and T_1 is the local temperature at which c_p^e is calculated [13]. The mixture molecular weight W_{mix} required for the state equation is calculated using

$$W_{\text{mix}} = \int_0^1 \int_0^1 \left(\sum_i \frac{Y_i}{W_i} \right)^{-1} \tilde{P}(\xi, \zeta) d\zeta d\xi. \quad (31)$$

The mean density is obtained using the ideal gas equation of state, $\bar{\rho} = \bar{p}W_{\text{mix}}/\tilde{T}R_0$, with \bar{p} being the thermodynamic pressure obtained from the simulation and $R_0 = 8314.5$ J/kmol-K is the universal gas constant. This expression is used to include compositional changes resulting from combustion. The Favre averaged scalar mass fractions are obtained using an integral equation similar to Eq. (29) and detailed description of these procedures are given in [13].

III. Test Case - a practical GT combustor

A. Geometry and Operating Conditions

Figure 1 shows the geometry of the burner assembly in a single combustor-can of a can-annular combustor for a high performance gas turbine [25]. The combustion characteristics at atmospheric conditions of this combustor-can, containing a center pilot burner and 8 main burners, were studied experimentally at MHI. The burners and air inlets are marked in Fig.1. The downstream geometry

of this combustor was modified to enable measurements of temperature and scalar concentrations. Operating conditions are listed in Table 1. The pilot burners were not operational for the test conditions studied here.

Table 1 Operating Condition.

Quantity	Values
Pressure	Atmospheric pressure
Inlet Air temperature	723 K
Inlet Air Flow rate	1.52 kg/s
Global Fuel/Air	3.01 %

Gaseous methane preheated to 473K and air with a small amount of water vapour preheated to 723K are injected separately into a chamber located upstream of the combustion chamber. The global fuel-air ratio is 3%. The total mass flow rates of fuel and air streams are given in Table 1. The Reynolds number based on main inlet velocity of 108 m/s is about 75000. The main premixed fuel streams with varying equivalence ratio and the non-premixed streams are marked in Fig.1. The non-premixed pilots are not operational for this study. Multiple fluid stream inlets are also present for cooling purposes, which are also included for the calculation reported here but are not shown in Fig.1 because of their relatively small sizes. The air inlets for film cooling are marked in Fig.1.

B. Experimental Measurement

The radial variations of temperature and scalar concentrations are measured at many axial locations. The measurement line is 15 degree from the mid-plane as shown in Fig.1. Sample probes can be inserted into the combustor at various axial locations as shown in Figure 1. Gaseous mixture is sampled from gas probes using vacuum pump. A Horiba PG240 analyser is used for the measurement of CO₂, NO_x and O₂. Horiba ES510 and VIA510-CO analysers are used for the measurement of CO. Water vapor in gas samples is eliminated by using drain cooler before measuring species concentrations.

The temperature is measured using thermocouples (type B, Pt-30Rh/Pt-6Rh) having a bead size of 0.3mm. The temperature measured using this thermocouple is corrected for heat losses due

to radiation using the balance between convective and radiative heat exchange at the thermocouple bead [26]. This gives

$$T_{\text{corrected}} = T_{\text{measured}} + \varepsilon\sigma(T_{\text{measured}}^4 - T_{\text{wall}}^4)/\alpha, \quad (32)$$

where $T_{\text{corrected}}$ is the corrected gas temperature, T_{measured} is the measured gas temperature, T_{wall} is the measured wall temperature, ε is the emissivity and $\sigma=5.67 \times 10^{-8} \text{ W/m}^2 - \text{K}^4$ is the Stefan-Boltzmann constant. The convective heat transfer coefficient α is obtained using the standard Nusselt number correlation for turbulent flow over a sphere. The contribution of gas phase radiation for radiative exchange is neglected because measurements are performed at atmospheric condition.

The measurement errors are due to the accuracy of measurement location of gas probes, water vapor contained in the sampled gas and the measurement instrument. The error related to location measurement can be position dependent. This is because of the fact that at upstream position, the gradient of temperature and concentration is larger than those in downstream positions. Assuming that the location uncertainty is about 1mm and a small amount of saturated vapor remained in the sampled gas even after drain cooling, the maximum error for temperature measurement is estimated between 1% (section E) and 4% (section A). The maximum error for concentration measurement is estimated to be between 4% (section I) and 10% (section A).

IV. Details of Numerical Simulation

Since the mean flow and flame characteristics inside the combustor-can are axisymmetric, only a 45 degree sector of the combustor-can is used for simulations. This sector includes one full main-burner and its associated gas paths as shown in Fig.1. A structured numerical grid involving about 2 million hexahedral cells is used. This mesh has a boundary layer grid near the walls which are treated to be adiabatic with no-slip condition. The film cooling paths and the thousands of perforated holes are explicitly included in the CFD mesh with about 7 grid points for each hole having non-zero exit velocity. The axial swirler located upstream of the combustor-can is excluded, but the effect of this swirler on the flow is specified through appropriate boundary conditions prescribing the velocity, mass flow rate, temperature and species profiles for the main and various inlets marked in Fig. 1. At the outlet, all the variables are specified to have zero axial gradient. These simplifications

reduce the computational cost considerably while retaining the essential flow features and giving good accuracy compared to experimental result as one shall see later in section V.

A look-up table listing various sources, sinks and mixture properties as noted in section II is computed *a priori* using appropriate laminar flames covering the full flammable range for the given temperature and pressure. This flamelet-table can be constructed using an arbitrarily complex chemistry and the GRI-Mech 3.0 involving 53 species and 325 reactions is used for the methane flames considered for this study. The number of points used for the five controlling parameters \tilde{Z} , \tilde{c} , $g_z = \widetilde{Z''^2}/(\tilde{Z}(1 - \tilde{Z}))$, $g_c = \widetilde{c''^2}/(\tilde{c}(1 - \tilde{c}))$ and $g_{cz} = \widetilde{Z''c''}/(\sqrt{\widetilde{Z''^2}\widetilde{c''^2}})$ of the look-up table are 24, 21, 21, 21 and 11 for the flame conditions expected inside the combustor. These points are distributed non-uniformly to ensure adequate resolution near $\tilde{c} = 0.6$ with large reaction rate. Linear interpolation in each of the controlling variable is used for the look-up process during simulations and the error in this interpolation procedure was assessed to be about 1% [13].

The PPF combustion model discussed in section 2 is implemented in a commercial CFD package, Fluent, using user defined functions (UDF) and scalars (UDS) as explained in [13, 27]. Six additional scalars transport equations for \tilde{Z} , \tilde{c} , $\widetilde{Z''^2}$, $\widetilde{c''^2}$, $\widetilde{c''Z''}$ and \tilde{h} given in Section II B are solved. The temperature and density fields are calculated in each iteration through the respective UDFs. Since the default combustion models in Fluent are not used here, combustion effects are coupled to the flow field through density variation which is computed through UDS and UDFs. This gives full control on the combustion modelling related equations and their solutions. Separate simulation using Fluent's EDC combustion model is also performed as a baseline case to evaluate the relative performance of the PPF combustion discussed earlier. The EDC model is chosen here because it is commonly used for gas turbine combustion calculation. The choice of turbulence model may have an impact on the combustion calculation as the $k-\epsilon$ has its known limitation for complex flows. More advanced model such as the Reynolds Stress model [28, 29] can provide improved results for complex flows. The influence of turbulence modelling is also investigated here by performing simulation with EDC and Reynolds Stress model (RSM) with a quadratic pressure-strain model.

The computational procedure is as followed. First, a non-reacting flow is computed using the boundary conditions given in Table 1. Then, the mixing of various inlet streams (scalar mixing)

is allowed to occur by including the appropriate scalar equations, which are treated to be simply convective-diffusive equations by setting the various chemical sources to be zero. In the third stage, a small flame kernel having burnt products of local mixture is specified for few cells located in a region with relatively low velocity and rich mixture close to the main inlet. This location is marked in Fig.2 to be discussed in detail later. This flame kernel is then allowed to evolve until a stable and converged solution is obtained. It is also found that the final solution is insensitive to the initial flame kernel location as long as it is placed within flammable mixture.

The parallel simulations are performed using 4 quad-core processors, Intel Xeon 3.0GHz with 8GB memory. The computational time to obtain a fully converged combustion solution is about 168 wall clock hours. Starting from a grid of 4M cells, grid sensitivity has been performed by systematically coarsening the grid and performing the combustion calculation with the EDC model until a grid independent insensitivity is noted. The results presented here are obtained from 2 millions cells.

V. Results and Discussion

A. General Features

Figure 2 present the temperature contour with velocity vectors and zero streamwise velocity ($\tilde{U}_x=0$) contour line, turbulent kinetic energy, mean mixture fraction and mean reaction rate in the mid-plane of the 45 degree sector model used here. The axial locations, marked A to E, are respectively at L_x/L of 0.04, 0.11, 0.18, 0.25 and 0.32, where L_x is the distance from the main premixed fuel inlet to the respective sections and $L=1.315\text{m}$ is the total length in this test case. These cross sections correspond to locations of experimental measurement shown in Fig.1. Section A corresponds to an upstream position of the flame anchoring and stabilising recirculation eddy. Section B is inside this eddy. Section C is located between downstream of this eddy and upstream of the first perforated plate injection holes. Sections D and E are in the middle and downstream of the perforated plate injection holes respectively. All these cross sections represent important locations where interesting flow-flame interaction are expected and also detailed comparison with experimental measurement will be discussed in the next section.

One observes from the temperature and mean reaction rate contours in Fig. 2 that the flame is established away from the main fuel injector and it stayed close to the pilot region in the combustor centre. The temperature and velocity become almost uniform by section E. The turbulent flame brush, marked by the temperature rise from 700K to about 1700K, is anchored by the recirculating hot products having \tilde{T} higher than 1500 K. This flame brush also corresponds to the region marked using $\tilde{c}=0.1$ and $\tilde{c}=0.9$ contours in Fig.2(c). The mean reaction rate is expected to be non-zero inside the flame brush, as seen in Fig.2(d). The intense reaction occurs in a region where the mixture ignited through the main premixed inlet meets the recirculating hot products. More specifically, the mean mixture fraction is about 0.03 for the region with peak reaction rate. This can be seen clearly by comparing Fig.2(a), 2(c) and 2(d).

The recirculation zone having burnt products is marked by the zero velocity contour in Fig.2(a). This zone extends axially from the pilot region to section C, and radially from the combustor centre to about 50% of the combustor radius. The shear is expected to be large in regions where this recirculation meets with various fluid streams entering the combustor. Thus the turbulent kinetic energy is large in this region as shown in Fig.2(b). This turbulent kinetic energy is one of the important quantities required for combustion modelling. It also facilitates mixing of species carried in various streams entering the combustor. The scalar mixing is usually studied using the mixture fraction field, shown in Fig.2(c). Inside most part of the recirculation zone, the mixture is relatively richer. The potential core of the main inlet stream extends upto section B. The mean reaction progress variable iso-contour $\tilde{c}=0.1$ and $\tilde{c}=0.9$, which marked the main flame brush position, is also shown in the mixture fraction contour. Together with the mean reaction rate contour, it is gathered that the flame locates downstream of the main fuel injector is stronger, due to locally richer mixture meeting the hot recirculating products, while downstream of the pilot the flame is much weaker, due to locally lean mixture and intense turbulent mixing of cold air and hot product. The mean reaction rate contour also indicates that the combustion is complete by about section D.

B. Flame Structure

Before moving on to detailed comparison of different models, the effect of turbulence modelling is first tested. Figure 3 presents a typical temperature variation obtained using EDC combustion model along with $k-\epsilon$ and RSM turbulence modelling. Only results from sections B and C, which are close to the strong recirculation region, are shown and the results at other sections are very similar. It is clear that the choice of turbulence modelling has only a minor effect in this case. Therefore, only EDC results for $k-\epsilon$ model are shown in the rest of the paper.

The quantitative performance of the PPF combustion model is evaluated in this section using measured flame brush structure. This analysis involves measured temperature and scalars concentration. The radial variation of averaged temperature and major scalar mole fraction on a dry basis are shown in Figs. 4 and 5 for various axial positions. The minor species results are to be discussed in the next section. Figure 4 presents these results for axial locations A to E marked in Fig. 2. Figure 5 presents the results for section I shown in Fig.1, which is the most downstream measurement position at 75% of the combustor length. The flow and mixture conditions at this section are representative of the combustor exit conditions. The computational results obtained using the EDC model are also included in these figure for comparison. The curves marked as ‘‘PPF NoCovar’’ in Figs. 4 and 5 denote numerical results obtained by assuming Z and c are statistically independent, i.e. $\widetilde{c''Z''} = 0$. The dry mole fraction of species i is calculated as $X_i/(1 - X_{\text{H}_2\text{O}})$, using computed mole fraction X_i . It is also worth noting that the temperature measurements from experiment are Reynolds averaged while the simulation results are Favre averaged. Previous studies [30] on Reynolds and Favre statistics showed that in premixed combustion under low swirl and low stratification condition, the difference between these two averages is within the error of measurement techniques and they are not significantly different from one another.

In order to assess the performance of different models, for each section, the normalised difference between simulation results and experimental data are quantified as

$$\mathcal{L}_2 = \frac{1}{N} \sum_{i=1}^N \sqrt{(X_i^{\text{Sim}} - X_i^{\text{Exp}})^2 / X_i^{\text{Exp}}}, \quad (33)$$

where N is the number of points for which the experimental measurement are available at each section. The maximum value of $\sqrt{(X_i^{\text{Sim}} - X_i^{\text{Exp}})^2 / X_i^{\text{Exp}}}$ within each sections is denoted as $\mathcal{L}_2^{\text{max}}$.

The following observations are made:

1. The centreline temperature obtained using the EDC model is good for the upstream location section A, although the mole fraction of O_2 and CO_2 obtained using this model for this position is poor as seen in Fig.4. For all other downstream locations, the temperature obtained from EDC model is not good. The mixture in the central region evolves too quickly toward its equilibrium as suggested by the over-estimate of temperature at sections B and C. The EDC model also fail to capture the temperature rise, and CO_2 and O_2 drop in the near-wall regions, as seen for sections E and I.
2. The PPF combustion model gives improved temperature compared to EDC model uniformly for all axial positions. At section A, both temperature and major species are captured accurately. The axial flame brush evolution is captured with improved accuracy. A reasonable agreement with experimental measurement can be seen for the centreline values and radial variation for sections B to I.
3. The PPF model also gives improved results in the near-wall region compared to the EDC model, although the near-wall combustion is under-predicted. This under-estimation is evident in section E shown in Fig.4, where near-wall reactions are possible because partly burnt mixture are injected through the perforated plate holes. This could be due to the limited treatment of the PPF combustion model for the near-wall processes.
4. The PPF model gives good agreement for temperature, and mole fraction of O_2 and CO_2 in the downstream position I, which represents the conditions of hot product coming out of the combustor.
5. A detailed examination (not shown here) of \mathcal{L}_2 and \mathcal{L}_2^{\max} shows that the species O_2 and CO_2 results from PPF models give similar or better results at all sections, except at section B for O_2 and section C for CO_2 . The worst case is shown in Table 2, which lists \mathcal{L}_2 and \mathcal{L}_2^{\max} for temperature and major scalar at section B and C. While \mathcal{L}_2 indicates temperature prediction for PPF model is better than EDC at these two positions, consistent with observation noted earlier, \mathcal{L}_2^{\max} given by PPF model is larger at section C. Furthermore, PPF model also gives a

larger \mathcal{L}_2^{\max} for CO₂ prediction at this position. A closer examination of Figure 4 shows that there is a local temperature increase at normalised height of ± 0.5 at section C, this causes a local peak in CO₂ values that contribute to the larger \mathcal{L}_2^{\max} value.

	Section	Temperature		O ₂		CO ₂	
		PPF	EDC	PPF	EDC	PPF	EDC
\mathcal{L}_2	B	0.06	0.19	0.09	0.05	0.29	0.70
	C	0.14	0.17	0.04	0.04	0.62	0.39
\mathcal{L}_2^{\max}	B	0.30	0.60	0.20	0.10	1.84	3.25
	C	0.55	0.46	0.07	0.04	2.08	1.72

Table 2 Worst case normalised difference.

One observation from Figs. 4 and 5 is that the simulation results obtained with and without the covariance, $\widetilde{c''Z''}$, are very similar for the condition investigated here. This perhaps becomes unsurprising when one examines the variances $\widetilde{Z''^2}$, $\widetilde{c''^2}$ and covariance $\widetilde{c''Z''}$ shown in Fig. 6. Due to the leanness of the reactant mixture, the range for $\widetilde{Z''^2}$ is very limited, as can be seen in Fig.6(a). Relatively larger values of $\widetilde{Z''^2}$ occur along the mixing layers next to the inlets, downstream of the pilot streams and upstream of recirculating flow. Figure 6(b) presents the variation of $\widetilde{c''^2}$ and this variation is large in region with intensive reaction rate, as one can see by comparing Figs. 6(b) and 2(d). The $\widetilde{c''^2}$ is significant only in regions upstream of section C, as most of the reaction is complete before this section. This correspondence is not surprising for premixed combustion. It is noted that the large $\widetilde{Z''^2}$ and $\widetilde{c''^2}$ are not occurring in the same region in general, except for a region located upstream of section A and close to the pilot. This behaviour of $\widetilde{Z''^2}$ and $\widetilde{c''^2}$ contributes to the overall small values of $\widetilde{c''Z''}$ as seen in Fig.6(c) for most part of the combustor. The correlation is therefore small for the conditions investigated here and thus the statistical independence of Z and c holds. Hence the results obtained using this assumption is very close to those obtained without this assumption.

C. CO and NOx Emission

Since the PPF combustion model includes detailed chemistry through pre-computed look-up table, intermediate species such as OH, CO and pollutants such as NOx can be obtained from simulation results. This is one key advantage of the tabulated chemistry approach used for the PPF model over the traditional EDC model, which usually assumes one-step fast chemistry and thus no intermediates or pollutants formation can be studied. Figure 7 presents the spatial variations of normalised dry volume fractions of CO and NOx in the combustor mid-plane. The quantities have been normalised by their global reference value respectively so that the normalised values are within the range of 0 to 1. One can see that the CO values are high along the flame brush with large reaction rate, marked in the figure using $\tilde{c} = 0.1$ and $\tilde{c} = 0.98$ iso-contour. This closely corresponds to region with intense reaction rate as in Fig. 2(d), which is not surprising as the progress variable definition includes Y_{CO} . Downstream of the perforated plates near sections D and G, there is small amount of CO present, which is likely due to CO accumulated in low velocity region coming from the mixture injected through the perforated plates. Figure 7(b) presents normalised dry volume fraction of NOx obtained directly from the flamelet table along with a temperature contour of 1700K. It is worth noting that this result include the species of NO and NO₂, and the major contribution is from NO. In general, high level of NOx is well within the region having mean temperature higher than 1700K. The highest level of NOx is observed in hot regions close to the first perforated plate between section C and D where some mixture is injected. These large values are usually expected from the flamelet approach because NOx does not obey the basic premises of flamelet assumption as the time scale for NOx is large. We shall revisit this point later.

Figure 8 shows the comparison of measured and computed radial variation of normalised dry CO volume fraction for axial positions A to I. The computed results with and without $\widetilde{c''Z''}$ are shown in Fig.8. Experimental measurement for section H is not available and thus it is not shown in the figure. The simulation results can capture the general trend reasonably well. There is no significant difference between the computed results with and without the covariance, similar to previous observation in Figs. 4 and 5 for temperature and major species mole fraction. At section A, the peak location is captured although the peak value is over-estimated. At positions

B and C, the computed peak location, peak values and the spread of radial variation agree well with experimental measurement. At downstream positions D and E, the peaks move away from the combustor centreline toward the wall. This variation is also captured reasonably by the PPF model although there are some under-estimation in the near-wall region. The model quantitatively captures the maximum CO formation at position F, and also reproduced the trend where CO formation gradually reduced at downstream positions G and I. Overall, the model prediction for CO is reasonable.

The NOx can form through several different paths as reviewed by Bowman [31]. The possible formation paths are: firstly, through the thermal or Zeldovich mechanism [32]; secondly, from the reaction of hydrocarbon radical and atmospheric nitrogen through the prompt mechanism [33]; thirdly, through nitrous oxide N_2O intermediate reaction [31] and finally the oxidation of possibly nitrogen compound in the fuel [34]. The last path is clearly not present for methane combustion studied here. The formation of NOx through other possible paths has generally a slow time scale and the residence time in a modern gas turbine combustor is short. In the flamelet model, there is an important assumption that chemistry is fast and this implies that NOx evaluation using flamelet solution can lead to incorrect results [35, 36].

An alternative approach commonly employed is to solve a transport equations for \tilde{Y}_{NO} as a post-processing step and this equation is given as

$$\frac{\partial \rho \tilde{Y}_{NO}}{\partial t} + \frac{\partial}{\partial x_i} (\bar{\rho} \tilde{u}_i \tilde{Y}_{NO}) = \frac{\partial}{\partial x_i} \left(\overline{\rho D \frac{\partial Y_{NO}}{\partial x_i}} - \bar{\rho} u_i' \tilde{Y}_{NO}' \right) + \bar{\omega}_{NO} \quad (34)$$

The reaction rate in $\bar{\omega}_{NO}$ can be computed in a similar way to the mean reaction rate through the flamelet library as in Eq.(1). A similar transport equation for \tilde{Y}_{NO_2} can be written. The assumptions in this model are, firstly, all species except NOx are formed on a sufficiently fast time scale so that solution from the flamelet library can be used; secondly, the model reaction rate for $\bar{\omega}_{NO}$ in Eq.(34) is considered second order accurate as the turbulent fluctuation in species are included in the flamelet library through the five controlling parameters discussed earlier. This model is implemented and the NOx transport equation is solved as a post-processing step.

Figure 9 shows the comparison of measured and computed normalised dry volume fraction of NOx at axial positions A to I. Again, the measured and computed values include NO and NO_2 .

Results from a total of four models are compared with experiment. They are the PPF model with $Z-c$ correlation, labelled as “PPF”, PPF model without $Z-c$ correlation, labelled as “PPF NoCovar” and models using Eq.(34) where $\bar{\omega}_{\text{NO}}$ is computed including and excluding the $Z-c$ correlation effects, labelled as “wNOx” and “wNOx NoCovar” respectively. The following points are noted.

- At upstream positions A and B, the flamelet table from the PPF model give the right NOx level at the centreline, but radial spread is under-estimated. From position B to D, there are two big over-estimated peaks at a height of about half radius from the centreline. A comparison to the temperature variation at these positions shown in Fig.4 reveals that they coincide with local mean temperature increase of the order of 100K. The flamelet results are very sensitive to this change as expected.
- In general, the flamelet PPF model over-estimates NOx level for all downstream position from C to I. The level of overestimation decreases as one moves in the downstream direction.
- At upstream position, the NOx values obtained through its transport equation are lower than the measured values, especially in the centerline. However, the radial spread profile is captured reasonably well, as seen at positions A to C. At positions C and D, there are also two notable peaks at height of half radius from combustor centreline due to the local temperature increases noted earlier. However, the level of overestimate in NOx is significantly reduced when the NOx transport equation is used as one would expect. At downstream positions, this approach gives very good quantitative agreement with experimental measurement, as seen for the positions E to I.

VI. Summary and Conclusion

In this study, simulation of turbulent premixed combustion with varying equivalence ratios in a gas turbine combustor with complex geometry is performed. The boundary conditions are specified using experimental measurement. The geometrical complexities are fully captured in the numerical grid used for the simulations. The flow and scalar mixing fields are captured using RANS approach with standard $k-\epsilon$ model. A commercial CFD tool, Fluent, is used for this study. However, the combustion is modelled using a flamelet based approach for partially premixed combustion including

the covariance, $\widetilde{c''Z''}$, of mixture fraction Z and progress variable c . This covariance, commonly neglected in previous studies, are included using a copula method following [12, 13]. Experimental measurement for temperature, major species, CO and NOx emission at atmospheric pressure is used to assess the model performance. It is found that this model gives temperature and major species variation inside the combustor in good agreement with experiment. The variation of CO estimated using this model is reasonable in showing the correct trends. The quantitative NOx prediction obtained using a transport equation for Y_{NO_x} agrees very well with measured values.

In this study, including the covariance in the joint PDF of Z and c does not improve the results. This is due to the narrow range of mixture fraction variation and its fluctuation present for the conditions investigated in this study. Furthermore, the pilot flame was not operational for this study, which has also limited the mixture fraction and progress variable fluctuation level. It is expected that the correlation effect would be important in the situation when rich mixture is injected in the pilot inlets and these rich premixed pilot flames act to support the lean main flame. This situation will be investigated in a future study. The partially premixed combustion model results are also compared with standard EDC model commonly used for gas turbine combustion calculation. This comparison showed that the partially premixed combustion model used in this study gives markedly improved results. The difference in CO values needs further investigation, which will be addressed in a future study.

References

- [1] Spalding, D. B., "Concentration fluctuations in a round turbulent free jet," *Chem. Eng. Sci.*, Vol. 26, 1971, pp. 95–107. doi:10.1016/0009-2509(71)86083-9.
- [2] Magnussen, B. and Hjertager, B., "On mathematical modelling of turbulent combustion with special emphasis on soot formation and combustion," *Proc. Combust. Inst.*, Vol. 16, 1977, pp. 719–727. doi:10.1016/S0082-0784(77)80366-4.
- [3] Bradley, D., Gaskell, P. H., and Lau, A. K. C., "A Mixedness-Reactedness Flamelet Model for Turbulent Diffusion Flames," *Proc. Combust. Inst.*, Vol. 23, 1990, pp. 685–692. doi:10.1016/S0082-0784(06)80317-6.
- [4] Bradley, D., Gaskell, P. H., and Gu, X. J., "Application of a Reynolds Stress, Stretched Flamelet, Mathematical Model to Computations of Turbulent Burning Velocities and Comparison with Experiments,"

- Combustion and Flame*, Vol. 96, 1996, pp. 221–248. doi:10.1016/0010-2180(94)90011-6.
- [5] Bradley, D., Gaskell, P. H., and Gu, X. J., “The Mathematical Modelling of Liftoff and Blowoff Turbulent Non-premixed Methane Jet Flames at High Strain Rates,” *Proc. Combust. Inst.*, Vol. 27, 1998, pp. 1199–1206. doi:10.1016/S0082-0784(98)80523-7.
- [6] Peters, N., *Turbulent Combustion*, Cambridge University Press, 2000.
- [7] Vervisch, L., Hauguel, R., Domingo, P., and Rullaud, M., “Three facets of turbulent combustion modelling: DNS of premixed V-flame, LES of lifted nonpremixed flame and RANS of jet-flame,” *J. Turbulence*, Vol. 5, 2004, pp. 004. doi:10.1088/1468-5248/5/1/004.
- [8] Swaminathan, N. and Bray, K. N. C., editors, *Turbulent Premixed Flames*, Cambridge University Press, 2011.
- [9] Ruan, S., Swaminathan, N., Bray, K. N. C., Mizobuchi, Y., and Takeno, T., “Scalar and its dissipation in the near field of turbulent lifted jet flame,” *Combustion and Flame*, Vol. 159, 2012, pp. 591–608. doi:10.1016/j.combustflame.2011.07.014.
- [10] Bray, K. N. C., Domingo, P., and Vervisch, L., “Role of the progress variable in models for partially premixed turbulent combustion,” *Combustion and Flame*, Vol. 141, 2005, pp. 431–437. doi:10.1016/j.combustflame.2005.01.017.
- [11] Ruan, S., Swaminathan, N., and Mizobuchi, Y., “Investigation of Flame Structure in Turbulent Lifted Jet Flame,” *Combust. Sci. Technol.*, Vol. 186, 2014, pp. 243–272. doi:10.1080/00102202.2013.877335.
- [12] Darbyshire, O. and Swaminathan, N., “A Presumed Joint PDF Model for Turbulent Combustion with Varying Equivalence Ratio,” *Combustion Science and Technology*, Vol. 184, 2012, pp. 2036–2067. doi:10.1080/00102200903476730.
- [13] Ruan, S., Swaminathan, N., and Darbyshire, O., “Modelling of turbulent lifted jet flames using flamelets: a priori assessment and a posteriori validation,” *Combust. Theory Model.*, Vol. 18, 2014, pp. 295–329. doi:10.1080/13647830.2014.898409.
- [14] Jones, W. P. and Launder, B. E., “The prediction of laminarization with a two equation model of turbulence,” *Int. J. Heat Mass Transfer.*, Vol. 15, 1972, pp. 301–314. doi:10.1016/0017-9310(72)90076-2.
- [15] Jones, W. P., “Turbulence modelling and numerical solution methods for variable density and combust- ing flows,” *Turbulent Reacting Flows*, edited by P. A. Libby and F. A. Williams, Academic Press, New York, 1994, pp. 309–347.
- [16] Zhang, S. and Rutland, C. J., “Premixed Flame Effects on Turbulence and Pressure-Related Terms,” *Combust. Flame*, Vol. 102, 1995, pp. 447–461. doi:10.1016/0010-2180(95)00036-6.

- [17] Bilger, R. W., “The structure of turbulent nonpremixed flames,” *Proc. Combust. Inst.*, Vol. 22, 1988, pp. 475–488. doi:10.1016/S0082-0784(89)80054-2.
- [18] Fiorina, B., Baron, R., Gicquel, O., Thevenin, D., Carpentier, S., and Darabiha, N., “Modelling non-adiabatic partially premixed flames using flame-prolongation of ILDM,” *Combust. Theory Model.*, Vol. 7, 2003, pp. 449–470. doi:10.1088/1364-7830/7/3/301.
- [19] Bray, K. N. C. and Libby, P. A., “Recent developments in the BML model of premixed turbulent combustion,” *Turbulent Reacting Flows*, edited by P. A. Libby and F. A. Williams, Academic Press, New York, 1994, pp. 115–151.
- [20] Kolla, H., Rogerson, J. W., Chakraborty, N., and Swaminathan, N., “Scalar Dissipation Rate Modeling and its Validation,” *Combustion Science and Technology*, Vol. 181, 2009, pp. 518–535. doi:10.1080/00102200802612419.
- [21] Domingo, P., Vervisch, L., and Bray, K. N. C., “Partially premixed flamelets in LES of non-premixed turbulent combustion,” *Combust. Theory Model.*, Vol. 6, 2002, pp. 529–551. doi:10.1088/1364-7830/6/4/301.
- [22] Domingo, P., Vervisch, L., and Réveillon, J., “DNS analysis of partially premixed combustion in spray and gaseous turbulent flame-bases stabilized in hot air,” *Combustion and Flame*, Vol. 140, 2005, pp. 172–195. doi:10.1016/j.combustflame.2004.11.006.
- [23] Domingo, P., Vervisch, L., and Veynante, D., “Large Eddy Simulation of a lifted methane jet flame in a vitiated coflow,” *Combustion and Flame*, Vol. 152, 2008, pp. 415–432. doi:10.1016/j.combustflame.2007.09.002.
- [24] Nguyen, P.-D., Vervisch, L., Subramanian, V., and Domingo, P., “Multidimensional flamelet-generated manifolds for partially premixed combustion,” *Combustion and Flame*, Vol. 157, 2010, pp. 43–61. doi:10.1016/j.combustflame.2009.07.008.
- [25] Tanimura, S., Nose, M., Ishizaka, K., Takiguchi, S., and Rodriguez, J., “Advanced Dry Low NOx Combustor for Mitsubishi G class gas turbine,” *Proceedings of ASME Turbo Expo 2008: Power for Land, Sea and Air*, Berlin, Germany, June 9-13 2008, pp. GT2008–50819.
- [26] Holman, J. P., *Heat Transfer*, McGraw-Hill, New York, USA, 9th ed., 2002.
- [27] Chen, Z., Ruan, S., and Swaminathan, N., “Simulation of turbulent lifted methane jet flames: Effects of air-dilution and transient flame propagation,” *Combustion and Flame*, 2014. doi:10.1016/j.combustflame.2014.09.010.
- [28] Hanjalić, K. and Jakirlić, S., “Second-Moment Turbulence Closure Modelling,” *Closure Strategies for Turbulent and Transitional Flows*, edited by B. E. Launder and N. D. Sandham, chap. 2, Cambridge

University Press, Cambridge, UK, 2002, pp. 47–101.

- [29] Manceau, R., Perrin, R., Hadžiabdić, M., and Benhamadouche, S., “Investigation of the interaction of a turbulent impinging jet and a heated, rotating disk,” *Physics of Fluids*, Vol. 26, 2014, pp. 035102. doi:10.1063/1.4867380.
- [30] Zhou, R., Balusamy, S., Sweeney, M. S., Barlow, R. S., and Hochgreb, S., “Flow field measurements of a series of turbulent premixed and stratified methane/air flames,” *Combustion and Flame*, Vol. 160, 2013, pp. 2017–2028. doi:10.1016/j.combustflame.2013.04.007.
- [31] Bowman, C. T., “Control of combustion-generated nitrogen oxide Emissions: technology driven by regulation,” *Proceedings of the Combustion Institute*, Vol. 24, 1992, pp. 859–878. doi:10.1016/S0082-0784(06)80104-9.
- [32] Zeldovich, Y. B., “The oxidation of nitrogen in combustion explosions,” *Acta Physicochim. USSR*, Vol. 21, 1946, pp. 577.
- [33] Fenimore, C. P., “Formation of nitric oxide in premixed hydrocarbon flames,” *Proceedings of the Combustion Institute*, Vol. 13, 1971, pp. 373–380. doi:10.1016/S0082-0784(71)80040-1.
- [34] Glarborg, P., Miller, J. A., and Kee, R. J., “Kinetic modeling and sensitivity analysis of nitrogen oxide formation in well-stirred reactors,” *Combustion and Flame*, Vol. 65(2), 1986, pp. 177–202. doi:10.1016/0010-2180(86)90018-0.
- [35] Bilger, R., “Reaction zone thickness and formation of nitric oxide in turbulent diffusion flames,” *Combustion and Flame*, Vol. 26, 1976, pp. 115–123. doi:10.1016/0010-2180(76)90061-4.
- [36] Ihmea, M. and Pitsch, H., “Modeling of radiation and nitric oxide formation in turbulent nonpremixed flames using a flamelet/progress variable formulation,” *Physics of Fluids*, Vol. 20, 2008, pp. 055110. doi:10.1063/1.2911047.

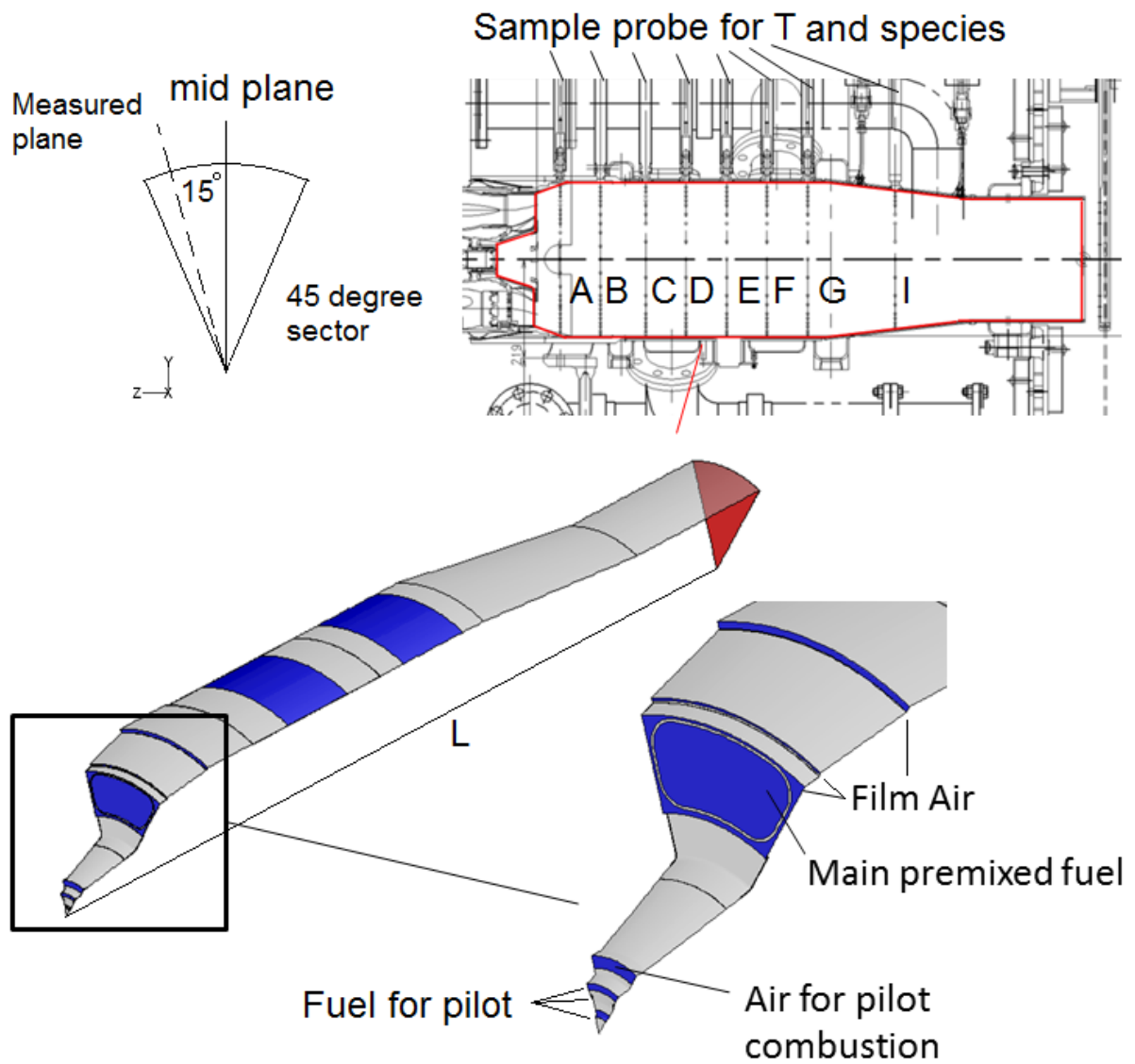


Fig. 1 Schematic of the computational domain and the mesh outline. The various important inlet and outlet streams are labeled.

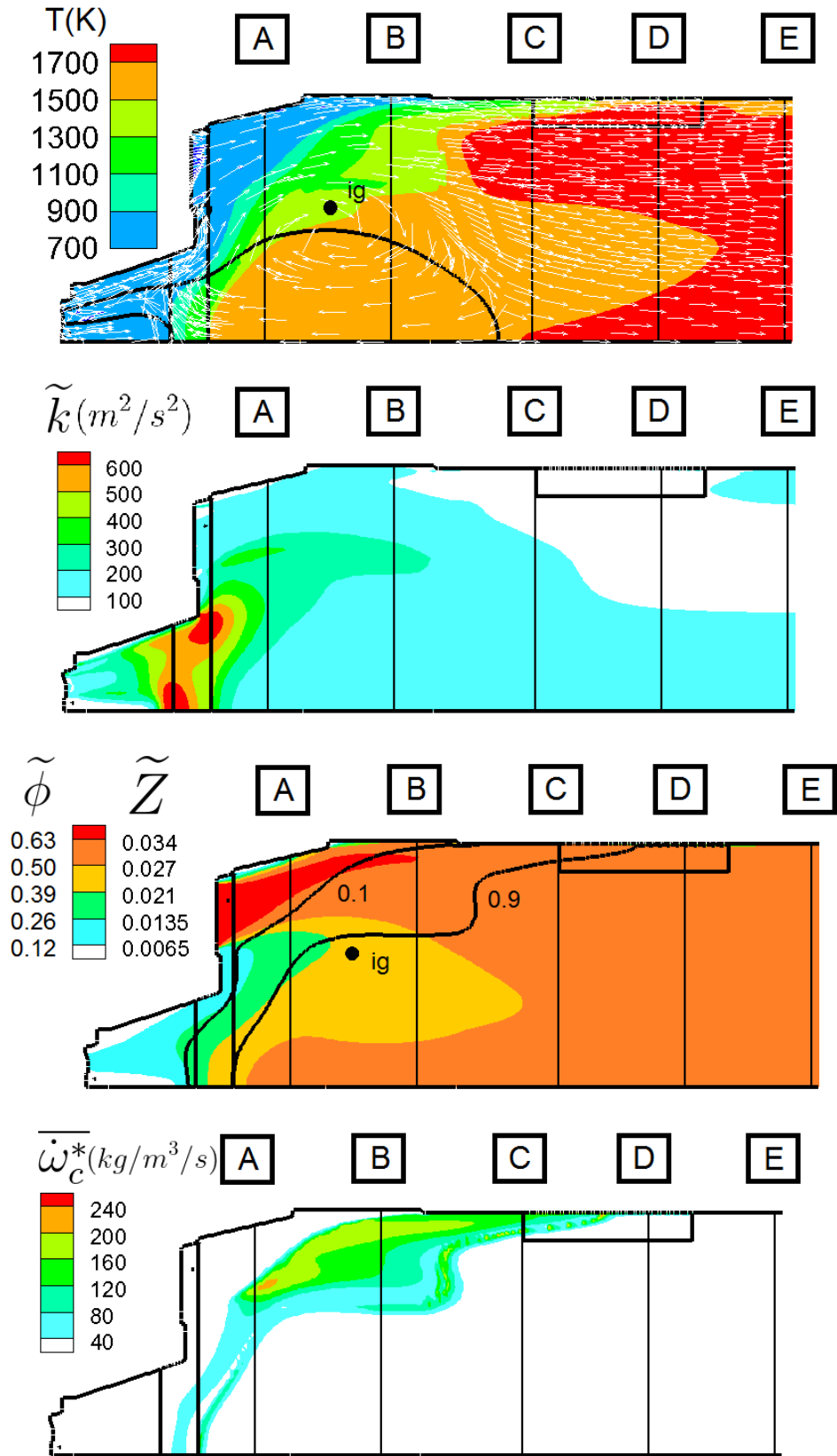


Fig. 2 (a) Velocity vector and temperature contour in the mid-plane. The zero velocity iso-line is labelled using black solid line. (b) Variation of Favre mean turbulent kinetic energy, (c) Favre mean mixture fraction with contour of $\tilde{z} = 0.1$ and $\tilde{z} = 0.9$ and (d) the mean reaction rate ($\text{kg}/\text{m}^3/\text{s}$) in the mid-plane. Ignition position is shown as black solid dot. Sections A to E are marked for further detailed comparison.

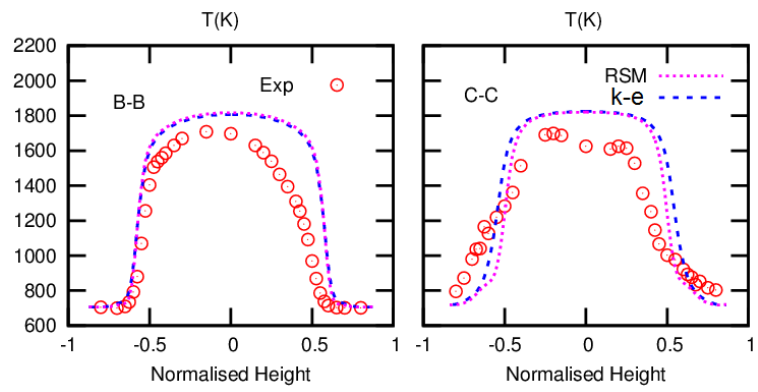


Fig. 3 Comparison of experimental data and computational results obtained using $k-\epsilon$ and RSM model for temperature at axial positions B and C. The EDC combustion model was used for these calculations.

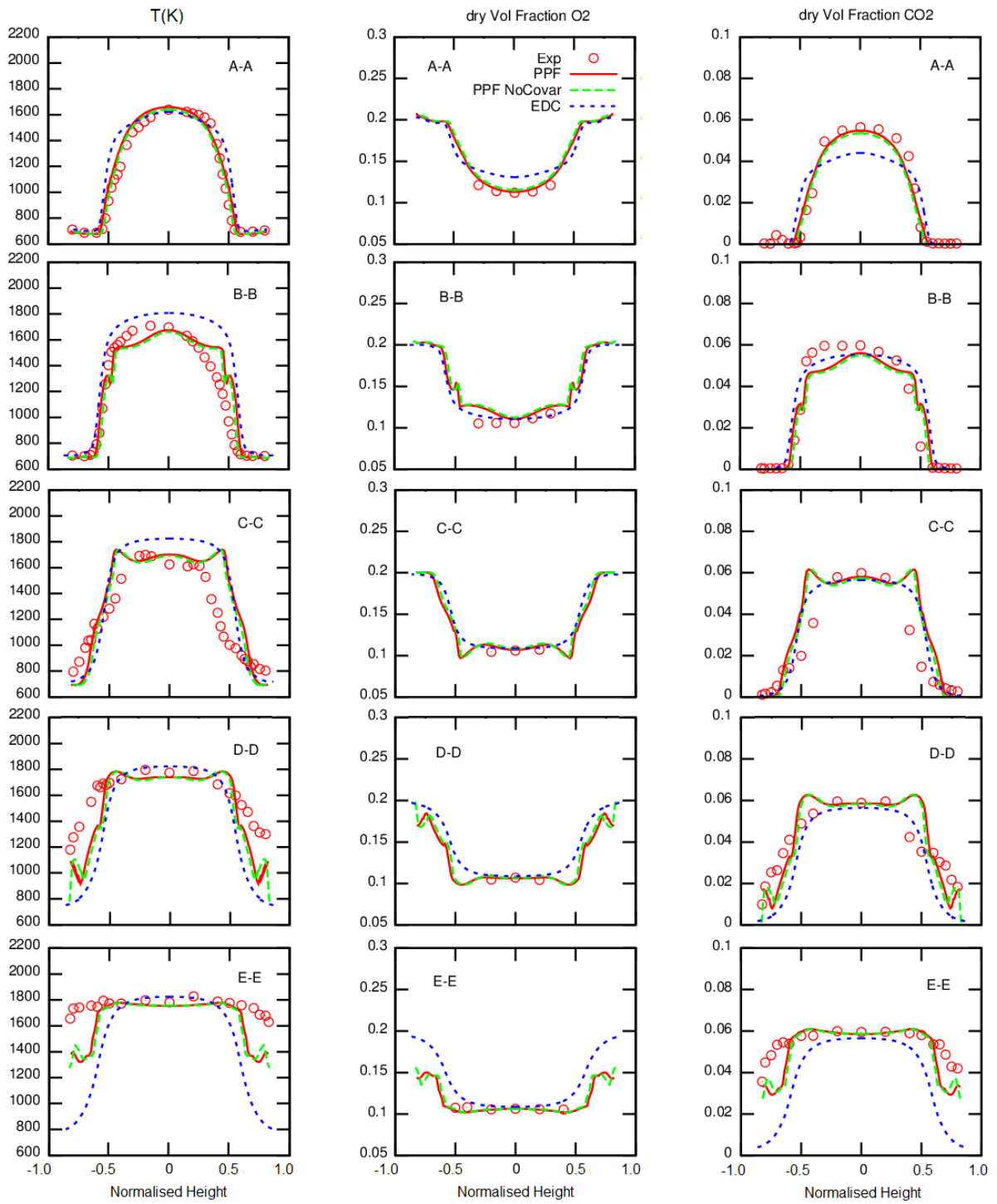


Fig. 4 Comparison of experimental and computational results for temperature (left), O₂ (middle) and CO₂ (right) for axial positions A to E.

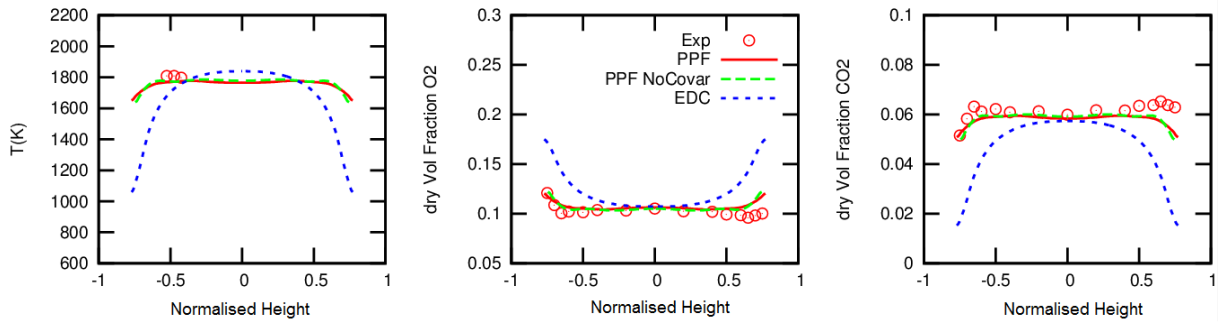


Fig. 5 Comparison of experimental and computational results for temperature (left), O₂ (middle) and CO₂ (right) for axial positions I close to combustor exit.

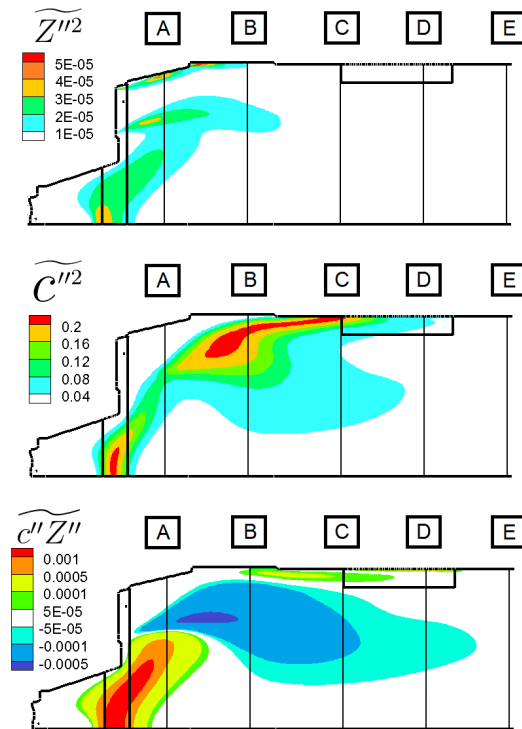


Fig. 6 Variation of (a) $\widetilde{Z''^2}$, (b) $\widetilde{c''^2}$ and (c) $\widetilde{c''Z''}$ in the combustor mid-plane.

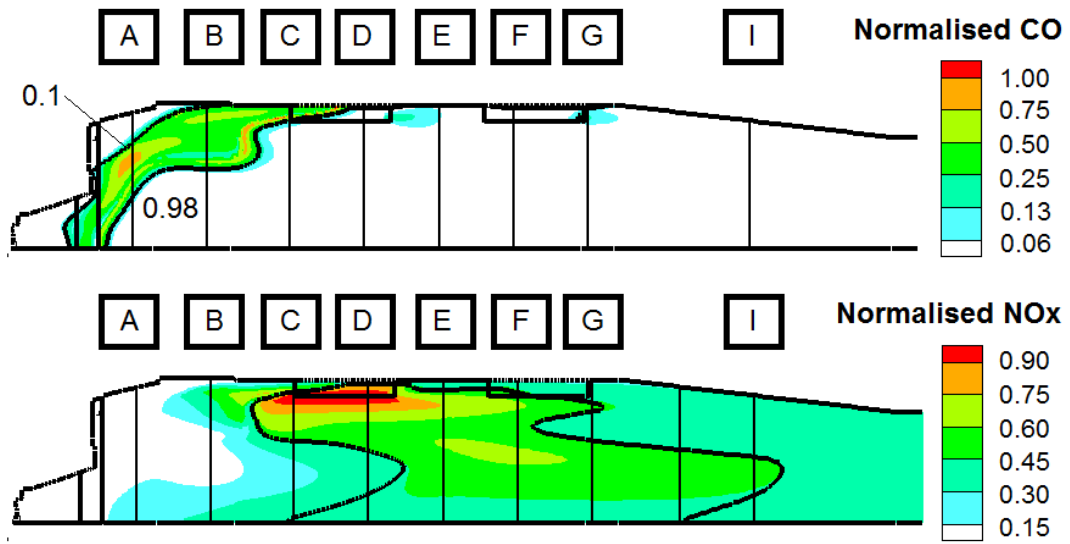


Fig. 7 The computed distributions of normalised dry volume fractions of (a) CO with iso-line of $\tilde{c} = 0.1$ and 0.98 and (b) NOx with iso-line of $\tilde{T} = 1700K$ in the combustor mid-plane for the PPF model.

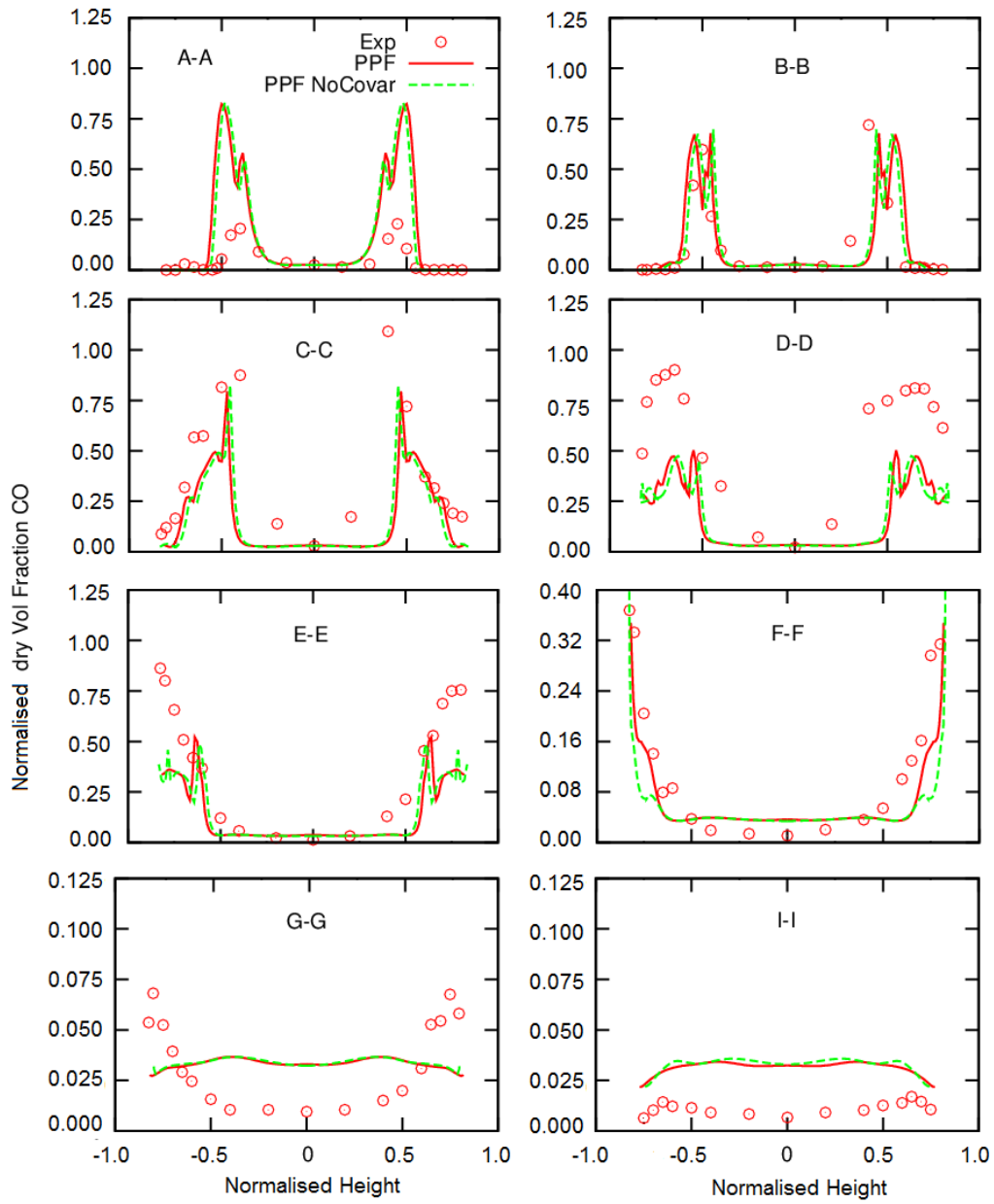


Fig. 8 Comparison experimental and computed radial variation of normalised CO dry volume fraction at different axial positions.

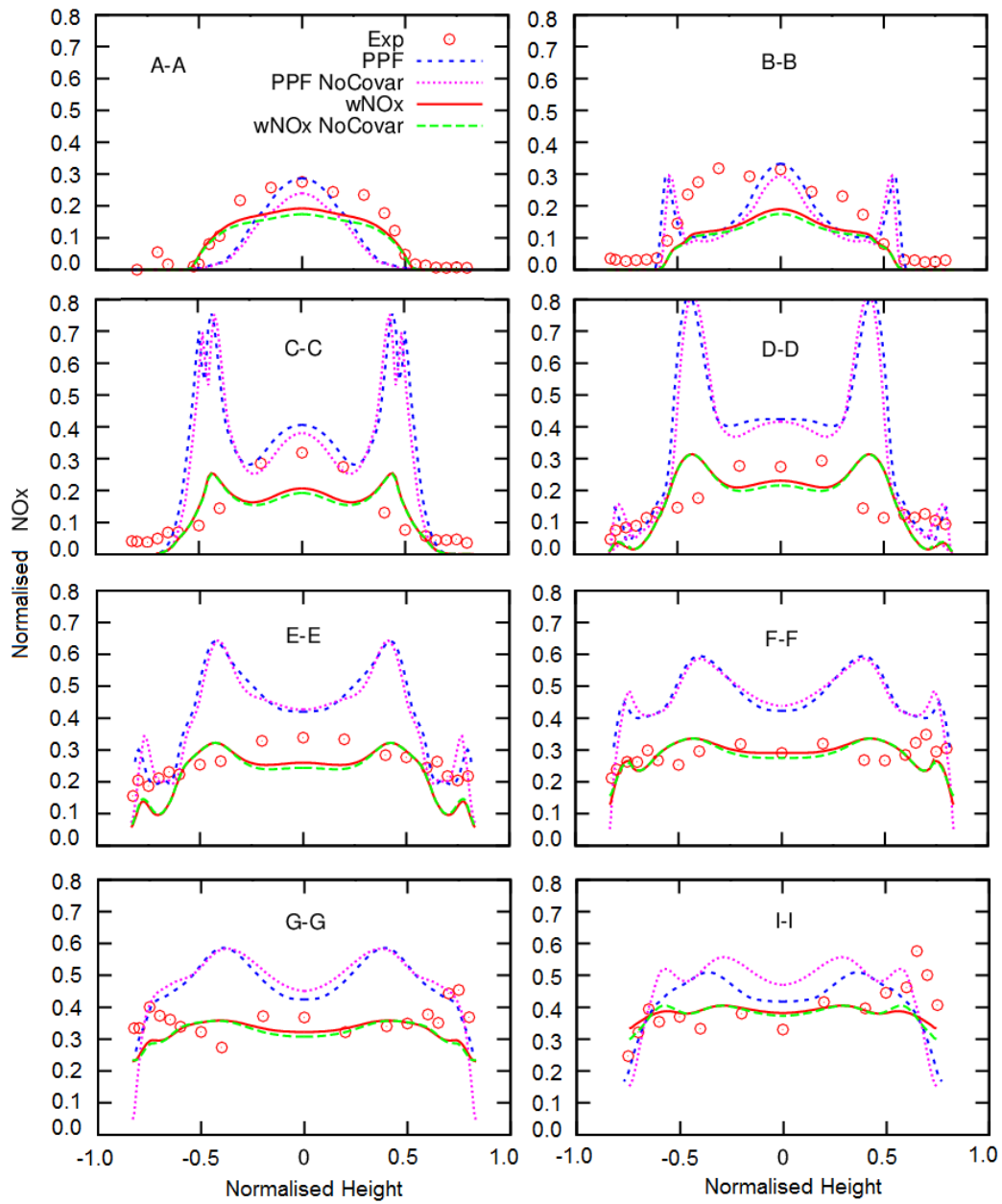


Fig. 9 Comparison of experimental and computational results for radial variation of normalised NOx at different axial positions.